INT. J. NUM. METH. HEAT FLUID FLOW, VOL. 4, 249–267 (1994)

FLOW CALCULATION IN A LOOP-SCAVENGED TWO-STROKE MOTORED ENGINE

Y.-Y. TSUI AND H.-P. CHENG

Department of Mechanical Engineering, National Chiao Tung University, Hsinchu 30049, Taiwan, R.O.C.

ABSTRACT

A multidimensional calculation method is used to investigate the flow in a motored two-stroke engine. The governing equations are written in a moving-coordinate system such that the grid can move with the piston. Grid lines are added into or deleted from the computational domain, depending on opening or closure of the ports. The EPISO algorithm is modified and adopted as the solution procedure. Calculations are performed on an engine of loop-scavenged type. Details of the gas exchange process and the flow structure in the cylinder are shown. The effects of the engine speed, inlet discharge coefficient and the angle of boost port are examined.

KEY WORDS Two-stroke engine Scavenging flow Numerical analysis

INTRODUCTION

The advantages of the two-stroke engine over the four-stroke engine are its mechanical simplicity, ease of maintenance and high power density. However, the use of two-stroke engines in modern power plants is mostly limited to light devices such as motorcycles, outboard motors, lawn mowers, etc. Its major drawback lies in the fact that considerable amount of fuel is lost due to the short circuiting of unburnt fresh charge to the exhaust. This inevitably causes a high level of hydrocarbon emission and deteriorates the fuel economy. To regain attraction for the two-stroke engine, one of the promising methods is the use of direct fuel injection[1–3]. With this method fuel-free fresh air is supplied during the gas-exchange process. The fuel is injected into the cylinder after most of the burnt gas is swept out of the cylinder or after the exhaust port is closed. As a consequence, the gas field built-up by the scavenging process will also be responsible for the fuel atomization, evaporation and mixing with the fresh charge. Therefore, a better understanding of the in-cylinder flow field becomes necessary.

In recent years, the newly developed technologies, such as the multidimensional calculation method and the laser doppler anemometry (LDA), have been adopted to study the flow in IC engines. The present study is concerned with the use of a multidimensional method to investigate the flow in a loop-scavenged two-stroke engine.

Sher[4,5] has used a quasi-three-dimensional model to simulate the gas exchange process in a loop-scavenged engine of Schnurle type. Since the flow is inevitably three-dimensional, not much of the flow structure was revealed in the studies. Details of the three-dimensional flow in the cylinder with a curved cylinder head were reported in the work of Ahmadi-Befrui *et al.*[6]. Their results showed that a loop flow and a pair of toroidal vortices are formed in the cylinder during the scavenge period and the vortex structure is responsible for impairment of the scavenging efficiency. The flow structure was found to be sensitive to the layout of the scavenge system.

9061–5539/94/030249–19$2.00

Received May 1991
Revised October 1993

Sweeney *et al.*[7] used the PHOENICS code[8] to investigate the scavenging characteristics of different port designs. The ranking of the cylinders based on their predictions was found in agreement with the experimental results. However, the predicted scavenging efficiencies for all cylinders were about 10% higher than the measured ones.

In the above calculations the efflux velocities at the scavenge ports were assumed to be uniformly distributed and directed in the angle of the port design. Smyth *et al.* adopted LDA to measure the efflux flow characteristics for a "cup-handle" type of scavenge port at different openings under either steady flow conditions[9] or low-speed motored conditions[10]. It was found that the uniform velocity profile was reasonably realistic. However, the flow issuing from the transfer ports did not flow in the port design direction at any port opening. There existed a good correlation between steady flow and motoring tests, justifying the use of steady flow information for dynamic simulation. With incorporation of the measured relationship between the efflux angle and the port opening under either steady or motoring conditions, the prediction of scavenge efficiency was significantly improved over that using the port-design angle as efflux angle. Epstein *et al.*[11], using the KIVA-II code[12], extended the computational domain into the exhaust and scavenge ports. This eliminates the need to specify boundary conditions at the openings of the ports. Their results showed that the flow field within the cylinder and the trapping efficiency are dependent on the angle of the boost port.

The solution method used in the works of Sher[4,5] and Ahmadi-Befrui[6] is similar to the RPM method developed by Gosman and his co-workers in the seventies[13] to calculate the flow in four-stroke engines. This method adopts an iterative procedure, like the one used in the SIMPLE algorithm[14], in each time step. Consequently, a large amount of computer time is consumed. To alleviate this problem, a non-iterative method, named EPISO, was later devised and applied to four-stroke engine calculations[15–19]. This method adopts the predictor-corrector concept of the PISO algorithm[20] and thus dispenses with iterations. Besides, it retains the fully implicit characteristics as the RPM method. Therefore, large time intervals are allowed in the calculations.

In this study, the flow in a loop-scavenged two-stroke engine with four transfer ports and one boost port is under investigation. The EPISO method is modified and applied. The flow characteristics in the cylinder, during the gas exchange period and the compression stroke, is examined in detail. Also investigated are the effects of the engine speed, the inlet discharge coefficients and the angle of the boost port.

MATHEMATICAL MODEL

Governing equations

The flow in the cylinder is inevitably unsteady, three-dimensional, turbulent and compressible. The governing equations are written in the density-weighted Favre-averaged form to account for density variations due to compressibility effects. The turbulence of the flow is modelled using the k–ε model of Launder and Spalding[21]. However, to account for the compressibility effects by the moving piston the Reynolds modification[22] is employed in the calculations. The coordinate system adopted is that, as shown in the schematic drawing of a grid layout in *Figure 1*, two coordinates ξ and η are orthogonal to each other and perpendicular to the cylinder axis z. Since the boundaries of the flow field in the cylinder is moving in accordance with the motion of the piston, the grid in the z direction is allowed to expand and contract with the piston motion in the following way.

As shown in *Figure 1*, there are two lines *KSP* and *KEP* corresponding to the upper edges of the scavenge and exhaust ports, respectively. The two lines divide the cylinder volume into three regions. Whenever the piston moves into one region, the grid lines in that region are set in motion with the piston but the grid lines in other regions are fixed without moving. Grid lines in regions I and II are added into or deleted from the computational domain depending

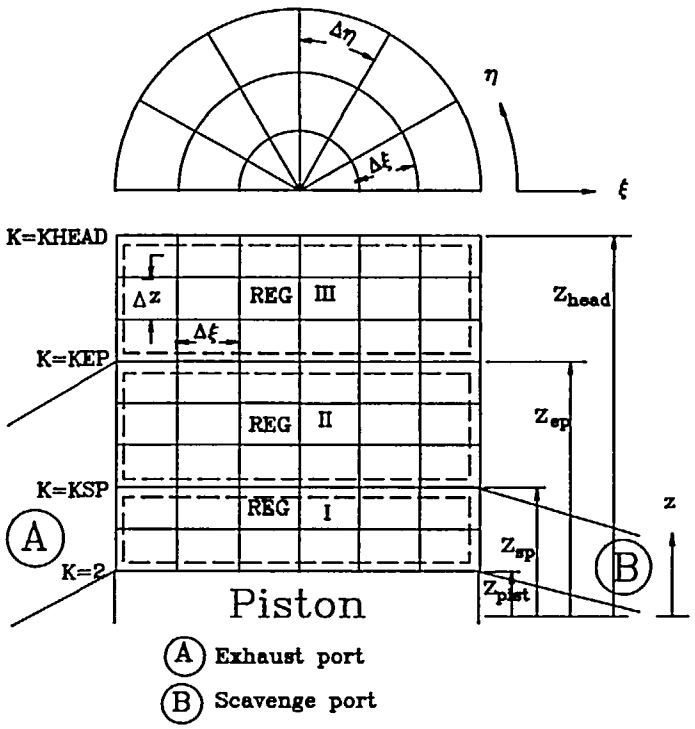

Figure 1 A typical grid layout

on whether the region is opened or closed at that instant. The addition or deletion of grid lines can be implemented simply by changing the starting K index in computations. For example, to discard the region I when the scavenging ports are closed the solution sweep starts from $K = KSP$ instead of $K = 2$. The grid velocity is defined as:

$$w_g = \frac{z_a - z_g}{z_a - z_{pist}} w_{pist} \tag{1}$$

where w_{pist} is the piston speed, z_g and z_{pist} are the instantaneous distances from a reference location to the grid line and the piston face, respectively, and z_a is the axial distance of the upper boundary of the considered region, i.e. $z_a = z_{sp}$, z_{ep} or z_{head} depending upon if the piston face is located in the region I, II or III (*Figure 1*). It is obvious that the grid velocity varies linearly from zero at the top to the piston speed at the bottom in the considered region. The final equations for the transport of the momentum, energy, turbulent kinetic energy k and its dissipation rate ε can be cast into a general form:

$$\frac{1}{\Delta V}\frac{\partial}{\partial t}(\rho\phi\Delta V) + \frac{1}{\Delta\eta}\frac{\partial}{\partial\xi}(\Delta\eta\rho u\phi) + \frac{1}{\Delta\xi}\frac{\partial}{\partial\eta}(\Delta\xi\rho v\phi) + \frac{\partial}{\partial\zeta}(\rho\hat{w}\phi)$$
$$= \frac{1}{\Delta\eta}\frac{\partial}{\partial\xi}\left(\Delta\eta\Gamma_\phi\frac{\partial\phi}{\partial\xi}\right) + \frac{1}{\Delta\xi}\frac{\partial}{\partial\eta}\left(\Delta\xi\Gamma_\phi\frac{\partial\phi}{\partial\eta}\right) + \frac{\partial}{\partial\zeta}\left(\Gamma_\phi\frac{\partial\phi}{\partial\zeta}\right) + S_\phi \tag{2}$$

where ΔV is the volume of the considered cell, u and v are the velocities in the ξ and η directions, respectively, and $\hat{w}$ is the axial velocity relative to the moving-grid velocity $\hat{w} = w - w_g$. In the above equation $\partial/\partial\zeta = 1/z_h \cdot \partial/\partial z$, where z_h represents $z_a - z_{pist}$ in the moving grid region and unity elsewhere. Details of Γ_ϕ and S_ϕ are given in *Table 1*.

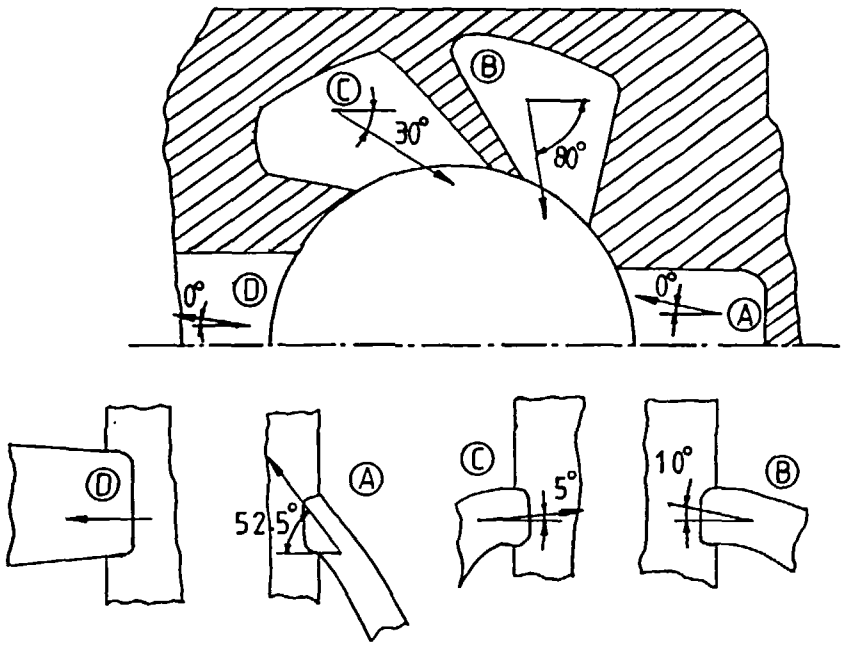

Figure 2 The flow angles through different ports

Boundary conditions

There are three kinds of boundaries encountered: solid walls, symmetry plane and port openings. At solid walls the wall function is used to bridge near-wall region[21]. Since the ports are arranged such that they are symmetric to a plane containing the cylinder axis and through the exhaust port, only half a cylinder is considered in calculations (see *Figure 2*). On the symmetry plane the velocity component normal to the plane (the velocity v) is set to zero and zero flux condition is imposed for all other variables. Velocities must be specified at the openings of the scavenge and exhaust ports. The mass flow rate through these ports are modelled by a one-dimensional flow as:

$$\dot{m} = C_d A(2\rho_u \Delta P)^{1/2} \tag{3}$$

Here C_d represents the discharge coefficient of the flow through the considered port, A is the area of the port opening, and ΔP is the effective pressure drop across the port determined from:

$$\Delta p = \left(\frac{\gamma}{\gamma-1}\right) p_u \left(\frac{p_d}{p_u}\right)^{2/\gamma} \left[1 - \left(\frac{p_d}{p_u}\right)^{(\gamma-1)/\gamma}\right], \qquad \text{for} \frac{p_d}{p_u} > 0.528 \tag{4}$$

$$\Delta p = \frac{\gamma}{2} p_u \left(\frac{2}{\gamma+1}\right)^{(\gamma+1)/(\gamma-1)}, \qquad \text{for} \frac{p_d}{p_u} \leqslant 0.528 \tag{5}$$

In the above, the subscripts "u" and "d" stand for the conditions upstream and downstream of the inlet or exhaust flow, respectively, and γ is the ratio of specific heats. Given as an example, for a flow into the cylinder through the scavenge ports, the upstream and downstream conditions are designated as those in the crankcase and cylinder, respectively.

The pressures in the crankcase and outside the exhaust port are assumed known. The average cylinder pressure can be obtained by solving simultaneous equations expressing the overall balance of mass and energy in the cylinder, as will be shown in the next section. The velocity

is assumed to be distributed uniformly over the opening area. The plug velocity profile is justified by the LDA measurement of Smyth *et al.*[9,10]. Their experiments also revealed that, as mentioned before, the flow entry angle varies with the port opening height. However, constant entry angles are assumed in the present calculations, as shown in *Figure 2*, because there is no experimental data available for the present case. It is inferred, based on the results of Smyth *et al.*, that the main features of the flow structure and the scavenging process are not altered, but the details are affected by this assumption.

The turbulent kinetic energy at the inlet is given as one percent of the inlet mean kinetic energy and the turbulent length scale is 4.5 percent of the port opening height. The temperature at the inlet and on all the walls is assumed to be 310°K.

METHOD OF SOLUTION

Discretization

The discretization is performed in the physical space following a finite volume approach. The staggered grid arrangement is used, in which the scalar properties are located at the center of each control volume and the velocity components are placed on the surrounding face points. The difference equations are obtained by taking integration of the differential equations over a control volume. Convection terms are approximated by the hybrid central/upwind differencing. The temporal difference used is the fully implicit scheme. The difference analogue of the equation (2) can be finally written as:

$$A_P\phi_P^n = \sum_c A_c\phi_c^n + S + A_P^o\phi_P^o \tag{6}$$

where the superscripts n and o denote the *new* and *old* time levels, respectively, the subscripts P stand for the considered nodal point P, the subscripts c denote the points surrounding the point P and the symbol $\sum$ represents the sum over the surrounding points, the coefficient simply designates $(\rho^o\Delta V^o)_P/\Delta t$, where ΔV is the volume of the cell.

It should be pointed out that the grid spacings in the axial direction in the computational region I or II defined in *Figure 1* are very small when the region is just opened or nearly closed. Thus the expansion ratio of the cells adjacent to the region interface becomes extremely large. This may deteriorate the computational accuracy as seen from the Taylor series truncation analysis.

EPISO algorithm

It is known that the continuity and momentum equations are strongly coupled through the dependence of velocity on the pressure, or vice versa. The PISO algorithm[20] handles the pressure-velocity coupling by an operator-splitting method involving a series of predictor and corrector steps. In this method, linearized momentum equations are first solved in a fully implicit fashion using the prevailing pressure field. The velocities and pressure are then adjusted via a number of corrector steps. It has been shown by Issa[20] that although the velocity field after the first corrector satisfies continuity, the momentum equations still suffer from mass imbalance left by the predictor velocities. This error diminishes when more correctors are used. As shown by Issa, the accuracy of the solution is within in the temporal truncation error after two correctors. Thus only two corrector steps are needed in the PISO algorithm.

Because of the displacement of the piston, the fluid in the cylinder is subject to bulk temporal changes in the pressure, temperature and density during the compression and expansion strokes. The changes, though smaller, are also existent during the gas exchange period due to the constrictions in the scavenge and exhaust ports. A process to treat the bulk changes is an

important feature of the EPISO method. The present treatment is somewhat different from that used in References 18 and 19 and will be given below.

In the following, each step of the EPISO method is briefly described. More details can be found in References 18 and 19.

Step 1. Grid adjustment: At each new time step the axial positions of the points in the moving-grid region are adjusted according to the prescribed grid velocity given in (1).

Step 2. Port flow calculation: The mass fluxes into and out of the cylinder are calculated according to equation (3), and then the flow velocities are imposed at the port openings as boundary conditions.

Step 3. Bulk adjustment: Before solving the flow field, the density, pressure, and temperature are globally adjusted such that the overall mass and energy in the cylinder are conserved. As in thermodynamics, the entire cylinder is treated as a single control volume. The conservation equations of mass and energy for such a control volume are given as:

$$\frac{dM_{cyl}}{dt} = \dot{m}_{in} - \dot{m}_{out} \tag{7}$$

$$\frac{dE_{cyl}}{dt} = \dot{m}_{in}e_{in} - \dot{m}_{out}e_{out} + \dot{Q} + \dot{W} \tag{8}$$

where M_{cyl} and E_{cyl} stands for the total mass and internal energy in the cylinder, respectively, the subscripts *in* and *out* denote the inlet and outflow fluxes, $\dot{Q}$ is the total heat flux across the cylinder wall, cylinder head and piston head, $\dot{W}$ is the work done by the piston motion. The two equations are discretized as follows:

$$M^n_{cyl} = M^o_{cyl} + (\dot{m}_{in} - \dot{m}_{out})\Delta t \tag{9}$$

$$E^n_{cyl} = E^o_{cyl} + (\dot{m}_{in}e_{in} - \dot{m}_{out}e_{out} + \dot{Q} + \dot{W})\Delta t \tag{10}$$

The cylinder mass and energy can be calculated through summation of the corresponding properties in all the cells in the cylinder. As an example:

$$M^n_{cyl} = \sum_i \rho^n_i \Delta V^n_i \tag{11}$$

$$E^n_{cyl} = \sum_i \rho^n_i e^n_i \Delta V^n_i \tag{12}$$

where the subscripts "i" refer to the ith cell of the computational grid. In the following, global increments of the pressure, temperature and density are sought. Let:

$$\rho^n_i = \rho_i + \rho^+ \tag{13}$$

$$p^n_i = p_i + p^+ \tag{14}$$

$$T^n_i = T_i + T^+ \tag{15}$$

where ρ_i, p_i and T_i are the prevailing local values and ρ^+, p^+ and T^+ the global increments. The equation of state is now introduced:

$$\rho^+ = \left(\frac{\partial \rho}{\partial p}\right)_T p^+ + \left(\frac{\partial \rho}{\partial T}\right)_p T^+$$

$$= \frac{1}{RT_i} p^+ - \frac{\rho_i}{T_i} T^+ \tag{16}$$

where the ideal gas is assumed. The internal energy is related to the temperature via the

thermodynamic relation $e = C_v T$. Substituting the above equations into equations (9) and (10) yields:

$$\rho^+ = \frac{1}{V^n_{cyl}}\left[-\sum_i \rho_i \Delta V^n_i + M^o_{cyl} + (\dot{m}_{in} - \dot{m}_{out})\Delta t\right] \tag{17}$$

$$p^+ = \frac{\sum_i \rho_i \Delta V^n_i e^n_i - E^o_{cyl} - (\dot{m}_{in} e_{in} - \dot{m}_{out} e_{out} + \dot{Q} + \dot{W})\Delta t}{w_{pist} A_{pist} \Delta t - \sum_i \dfrac{e_i \Delta V^n_i}{RT_i}} \tag{18}$$

where A_{pist} is the cross-sectional area of the piston head. These bulk adjustments provide an initial estimate of the pressure level for the new time step.

Step 4. Momentum predictor: The discretized momentum equation for each velocity component u_i is linearized by evaluating the coefficients A_p and A_c and the source S from the old-time-level velocities and prevailing density. In the following expression the pressure term is separated from the source and the prevailing pressure field is denoted as p^*:

$$A^{u_i}_P u^*_{iP} = \sum_c A^{u_i}_c u^*_{ic} - a_i \Delta_i p^* + S^{u_i} + A^o_P u^o_{iP} \tag{19}$$

where the symbol Δp is the difference form of the pressure gradient for the u_i momentum equation and a_i is the area of the considered cell face. By solving the linear set of equations the first approximation of velocity u_i^* is obtained.

Step 5. First momentum corrector: The first momentum corrector equations are written as:

$$\frac{A^{u_i}_P}{\rho^*_P} \rho^{**}_P u^{**}_{iP} = \sum_c A^{u_i}_c u^*_{ic} - a_i \Delta_i p^{**} + S^{u_i} + A^o_P u^o_{iP} \tag{20}$$

in which the symbols "**" designate the corrected values. By subtracting the predictor equation (19) leads to:

$$\rho^{**}_P u^{**}_{iP} = \rho^*_P u^*_{iP} - \rho^*_P A_i \Delta_i p' \tag{21}$$

where p' is the pressure correction ($\equiv p^{**} - p^*$). With a linearized equation of state:

$$\rho^{**}_P = \rho^*_P + \frac{1}{RT^*_i} p'_P \tag{22}$$

a Poisson type difference equation for p' can be derived by taking divergence of the above correction equation and forcing ρ^{**} and u_i^{**} to satisfy the continuity equation:

$$A^p_P p'_P = \sum_c A_c p'_c + S^p \tag{23}$$

Once p' is obtained, the pressure is upgraded to p^{**} level and the density and velocities are corrected accordingly via equations (22) and (21).

Step 6. Energy calculation: The energy equation is solved in this step.

Step 7. Second momentum corrector: The velocities u_i^{**} satisfy the continuity constraint. However, the neighbouring-points contributions to the momentum equation in the first corrector equation include the velocity field u_i^* which does not satisfy the continuity. In this step, velocities, denoted by ***, are sought by solving the following equation:

$$\frac{A^{u_i}_P}{\rho^*_P} \rho^{***}_P u^{***}_{iP} = \sum_c A^{u_i}_c u^{**}_{ic} - a_i \Delta_i p^{***} + S^{u_i} + A^o_P u^o_{iP} \tag{24}$$

In the same way as in the first corrector, a pressure correction equation for p'' ($\equiv p^{***\prime} - p^{**}$) can be derived in the similar form as equation (23) with the same coefficients, but different source terms. After obtaining p'', the pressure, density and velocities are corrected to the *** level.

Step 8. Turbulence predictor step: The predictor step entails sequential solutions of the k- and ε-equations to yield an initial estimate of the turbulence and dissipation.

Step 9. Turbulence corrector step: The k- and ε-equations are strongly coupled through their source terms, i.e. the generation and dissipation terms. In this step, the contributions from neighbouring points to the discrete k- and ε-equations through the convection and diffusion are maintained at the predictor level and the source terms are upgraded. In this way the equations at each mesh point are decoupled with the equations for the surrounding points. The resulting equations are two second-degree equations[18,19] which can be solved by, for example, the Newton–Raphson method. It was shown[18] that each of the equations represents a set of hyperbolic curves. There exists four roots determined by the intersections of the curves. One trivial solution is that $k = 0$ and $\varepsilon = 0$. There are two non-physical roots with negative k and/or ε. The existence of the multiple roots may cause an iterative solution procedure to select one of the unrealistic solutions. Therefore it is necessary that a *good* initial guess must be provided.

Step 10. Fresh-charge-concentration calculation: It is important to examine the scavenging efficiency for two-stroke engines. Therefore, a transport equation for fresh-charge-concentration is solved after the entire flow field is upgraded to its final level. The mass fraction of fresh air entering at the scavenging ports is assigned the value of unity as the inlet boundary condition and that of residual gas initially residing in the cylinder is zero.

The above ten steps complete the solution procedure in one time step. The calculation is then advanced to the next time step and re-commenced from the first step.

RESULTS

The engine tested is of the loop-scavenged type equipped with flat piston and cylinder heads and two kinds of transfer port (denoted as ports B and C in *Figure 2*) and one boost port (denoted as port A in *Figure 2*). The design angles of the ports are displayed in *Figure 2*. The other engine specifications are given in *Table 2*.

The arrangement of the intake ports around the cylinder liner is symmetric with respect to an axial plane through the exhaust port. Therefore the calculation is confined within half the cylinder domain. A typical grid used in the calculations is shown in *Figure 3*. To test the effects of grid density on the predictions the variation of the cylinder-averaged fresh-charge-concentration against crank angle predicted using four different grids is shown in *Figure 4*. As seen from the figure, the level of concentration in the cylinder is lower for high grid densities after the scavenging process is completed. This simply reflects that with high grid density the mixing of fresh air with residual gas is enhanced and, thus, more fresh charge escapes out of the cylinder during the scavenging period due to short circuit as will be seen later. In the figure the difference between the predictions by the $25 * 45 * 45$ grid and the $35 * 55 * 55$ grid is minor. Although it cannot be concluded that these results have been grid independent, they may be accurate to some certain levels. Owing to the limitation on access to large computer resource, the $25 * 45 * 45$ grid was finally adopted in the calculations throughout this study.

For the calculation of mass fluxes through the scavenge ports, the pressure in the crankcase is set at 0.12 MPa and the discharge coefficient at 0.7. As for the exhaust flow, the outside air is at atmospheric condition and the discharge coefficient is 0.9. All calculations commence from EPO (i.e. 108° CA) and end at TDC. Initially, the flow is assumed to be quiescent in the cylinder. The initial pressure is 0.25 MPa.

In the following, the flow quantities such as the velocity of the flow through the ports and

Table 1 Diffusion coefficients and source terms

ϕ	Γ_ϕ	S_ϕ
u	μ_t	$-\frac{\partial p}{\partial \xi}+\frac{1}{\Delta\eta}\frac{\partial}{\partial \xi}\left[\Delta\eta\mu_t\left[\frac{\partial u}{\partial \xi}+2\frac{v}{\Delta\xi}\frac{\partial \Delta\xi}{\partial \eta}\right]\right]+\frac{\partial}{\partial \xi}\left[-\frac{2}{3}(\mu_t\nabla_i u_i+\rho k)\right]$ $+\frac{1}{\Delta\xi}\frac{\partial}{\partial \eta}\left[\Delta\xi\mu_t\left[\frac{\partial v}{\partial \xi}-\frac{v}{\Delta\eta}\frac{\partial \Delta\eta}{\partial \xi}-\frac{u}{\Delta\xi}\frac{\partial \Delta\xi}{\partial \eta}\right]\right]+\frac{\partial}{\partial \zeta}\left[\mu_t\frac{\partial w}{\partial \xi}\right]$ $+\frac{\mu_t}{\Delta\xi}\left[\frac{\partial v}{\partial \xi}+\frac{\partial u}{\partial \eta}-\frac{v}{\partial \eta}\frac{\partial \Delta\eta}{\partial \xi}-\frac{u}{\Delta\xi}\frac{\partial \Delta\xi}{\partial \eta}\right]\frac{\partial \Delta\xi}{\partial \eta}-\frac{\rho uv}{\Delta\xi}\frac{\partial \Delta\xi}{\partial \eta}$ $-\frac{2\mu_t}{\Delta\eta}\left[\frac{\partial v}{\partial \eta}+\frac{u}{\Delta\eta}\frac{\partial \Delta\eta}{\partial \xi}\right]\frac{\partial \Delta\eta}{\partial \xi}+\frac{\rho v^2}{\Delta\eta}\frac{\partial \Delta\eta}{\partial \xi}$
v	μ_t	$-\frac{\partial p}{\partial \eta}+\frac{1}{\Delta\eta}\frac{\partial}{\partial \xi}\left[\Delta\eta\mu_t\left[\frac{\partial u}{\partial \eta}-\frac{v}{\Delta\eta}\frac{\partial \Delta\eta}{\partial \xi}-\frac{u}{\Delta\xi}\frac{\partial \Delta\xi}{\partial \eta}\right]\right]$ $+\frac{1}{\Delta\xi}\frac{\partial}{\partial \eta}\left[\Delta\xi\mu_t\left[\frac{\partial v}{\partial \eta}+\frac{2u}{\Delta\eta}\frac{\partial \Delta\eta}{\partial \xi}\right]\right]+\frac{\partial}{\partial \eta}\left[-\frac{2}{3}(\mu_t\nabla_i u_i+\rho k)\right]$ $+\frac{\partial}{\partial \zeta}\left[\mu_t\frac{\partial w}{\partial \eta}\right]+\frac{\mu_t}{\Delta\eta}\left[\frac{\partial v}{\partial \xi}+\frac{\partial u}{\partial \eta}-\frac{v}{\Delta\eta}\frac{\partial \Delta\eta}{\partial \xi}-\frac{u}{\Delta\xi}\frac{\partial \Delta\xi}{\partial \eta}\right]\frac{\partial \Delta\eta}{\partial \xi}-\frac{\rho uv}{\Delta\eta}\frac{\partial \Delta\eta}{\partial \xi}$ $-\frac{2\mu_t}{\Delta\xi}\left[\frac{\partial u}{\partial \xi}+\frac{v}{\Delta\xi}\frac{\partial \Delta\xi}{\partial \eta}\right]\frac{\partial \Delta\xi}{\partial \eta}+\frac{\rho u^2}{\Delta\xi}\frac{\partial \Delta\xi}{\partial \eta}$
$\hat{w}$	μ_t	$-\frac{\partial p}{\partial \zeta}+\frac{1}{\Delta\eta}\frac{\partial}{\partial \xi}\left[\Delta\eta\mu_t\frac{\partial u}{\partial \zeta}\right]+\frac{1}{\Delta\xi}\frac{\partial}{\partial \eta}\left[\Delta\xi\mu_t\frac{\partial v}{\partial \zeta}\right]+\frac{\partial}{\partial \zeta}\left[\mu_t\frac{\partial w}{\partial \zeta}-\frac{2}{3}(\mu_t\nabla_i u_i+\rho k)\right]$ $-\left[\frac{1}{z_h}\frac{\partial(\rho z_h w_g)}{\partial t}+\frac{1}{\Delta\eta}\frac{\partial}{\partial \xi}\left[\Delta\eta\rho uw_g-\Delta\eta\mu_t\frac{\partial w_g}{\partial \xi}\right]\right.$ $\left.+\frac{1}{\Delta\xi}\frac{\partial}{\partial \eta}\left[\Delta\xi\rho vw_g-\Delta\xi\mu_t\frac{\partial w_g}{\partial \eta}\right]+\frac{\partial}{\partial \zeta}\left[\rho\hat{w}w_g-\mu_t\frac{\partial w_g}{\partial \zeta}\right]\right]$
e	$\frac{\mu_t}{\sigma_{e,t}}$	$p\nabla_i u_i$
k	$\frac{\mu_t}{\sigma_k}$	$\mu_t G-\rho\varepsilon$
ε	$\frac{\mu_t}{\sigma_\varepsilon}$	$C_1\mu_t G\frac{\varepsilon}{k}-C_2\rho\frac{\varepsilon^2}{k}+C_3\rho\varepsilon\nabla_i u_i$

Note:

(1) $$\nabla_i u_i=\frac{1}{\Delta\eta}\frac{\partial}{\partial \xi}(\Delta\eta u)+\frac{1}{\Delta\xi}\frac{\partial}{\partial \eta}(\Delta\xi v)+\frac{\partial}{\partial z}(w)$$

(2) $$\mu_t G=\frac{1}{2\mu_t}[T_{\xi\xi}^2+T_{\eta\eta}^2+T_{zz}^2+2(T_{\xi\eta}^2+T_{\xi z}^2+T_{\eta z}^2)]-\frac{2}{3}(\mu_t\nabla_i u_i+\rho k)\nabla_i u_i$$

where

$$T_{\xi\xi}=2\mu_t\left[\frac{\partial u}{\partial \xi}+\frac{v}{\Delta\xi}\frac{\partial \Delta\xi}{\partial \eta}\right],\qquad T_{\xi\eta}=\mu_t\left[\frac{\partial v}{\partial \xi}+\frac{\partial u}{\partial \eta}-\frac{v}{\Delta\eta}\frac{\partial \Delta\eta}{\partial \xi}-\frac{u}{\Delta\xi}\frac{\partial \Delta\xi}{\partial \eta}\right]$$

$$T_{\eta\eta}=2\mu_t\left[\frac{\partial v}{\partial \eta}+\frac{u}{\Delta\eta}\frac{\partial \Delta\eta}{\partial \xi}\right],\qquad T_{\xi z}=\mu_t\left[\frac{\partial w}{\partial \xi}+\frac{\partial u}{\partial z}\right]$$

$$T_{zz}=2\mu_t\frac{\partial w}{\partial z},\qquad T_{\eta z}=\mu_t\left[\frac{\partial w}{\partial \eta}+\frac{\partial v}{\partial z}\right]$$

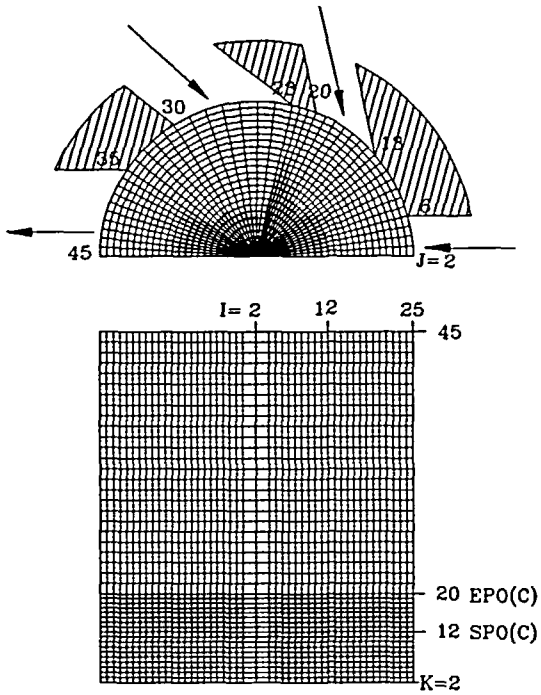

Figure 3 Computational grid

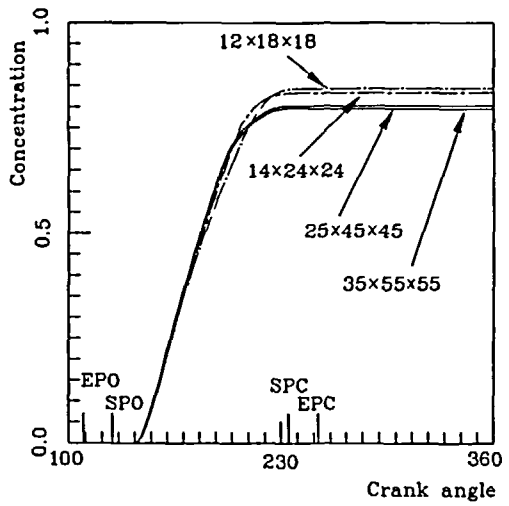

Figure 4 Grid refinement test

the cylinder pressure are presented. Then the plots of velocity vector and fresh-charge-concentration contour are displayed. This is followed by a parametric study in which the effects of the engine speed, inlet discharge coefficient, and the angle of the boost port are examined.

The temporal variation of the inlet and outlet radial velocities through the scavenge and exhaust ports, calculated using the method described above, is shown in *Figure 5*. The velocities

Table 2 Engine specification

Cylinder bore	74 mm
Clearance	8.15 mm
Stroke	75 mm
Compression ratio	10.2
Engine speed	3000 rpm
Exhaust port opening	108° CA (ATDC)
Exhaust port closure	252° CA (ATDC)
Scavenge port opening	126° CA (ATDC)
Scavenge port closure	234° CA (ATDC)

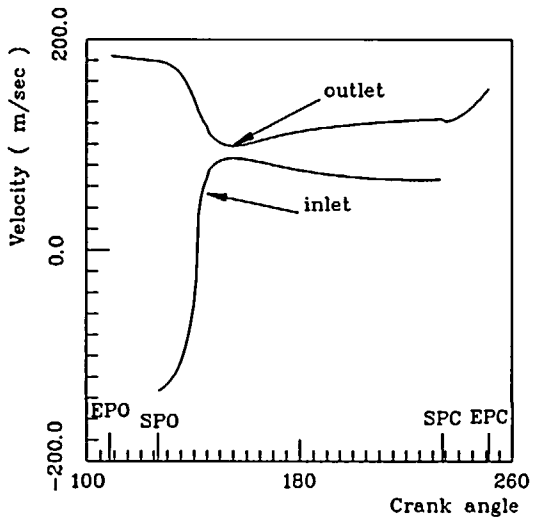

Figure 5 Temporal variation of inlet and outlet velocities through the scavenge and exhaust ports

are related to the pressure in the cylinder, which is displayed in *Figure 6*. After the exhaust port is opened, the gas in the cylinder is expelled into the exhaust port at a high speed. During the period from EPO to SPO, the change of the outlet velocity is small despite the rapid decrease of the cylinder pressure. After the scavenge ports are opened, the decreasing rate of the outlet velocity is accelerated while that of the cylinder pressure remains high. Since the cylinder pressure at SPO is higher than the prescribed pressure in the crank case, the gas is also expelled through the scavenge ports, resulting in negative inlet velocity. The sharp decrease of the cylinder pressure continues until about 142° CA. It is followed by levelling off of the pressure with slight variation throughout the remaining scavenge period. It has a minimum value of 0.1089 MPa at 156° CA which corresponds to the time of maximum inlet velocity and minimum outlet velocity. It can be observed that although the change of the cylinder pressure is small during the period, its effects on the variation of flow velocity is still substantial. After the scavenging ports are closed, the cylinder pressure is recovered gradually and the outlet velocity increases sharply. In the compression stroke, the cylinder pressure increases until TDC. Also presented in *Figure 6* during the compression period is a curve corresponding to isentropic compression. The difference between the predicted and the isentropic value is due to the heat transfer out of the cylinder.

To illustrate the flow structure, the plots of velocity vector and fresh-charge-concentration contour are presented at selected axial planes and crank angles. The axial planes are referenced by their J indices as defined in *Figure 3*. To calculate the fresh-charge concentration one more

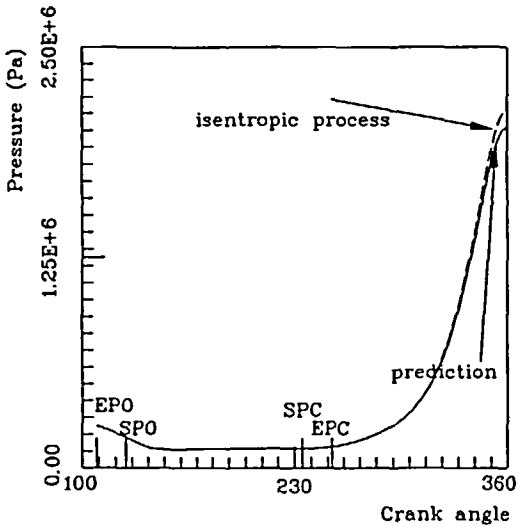

Figure 6 Temporal variation of cylinder pressure

transport equation is needed to be solved. The value of zero concentration is assigned to the residual gas in the cylinder at EPO as initial condition and the value of unity to the fresh charge emerging from the scavenging ports. The residual gas and the fresh charge are assumed to have the same molecular weight. Therefore the equation for the concentration is decoupled with the other equations.

The flow field for 180° CA is illustrated in *Figure 7*. The vector plots (*Figure 7a*) showed that the fresh charge issuing from the boost port (J = 2 plane) is directed upward toward the cylinder head and the flow out of the two transfer ports (J = 18 and 27 planes) merge at the center region as a rising stream also toward the cylinder head. A toroidal vortex is formed at both sides of the rising stream. The gas in the region near the exhaust port is expelled. The distribution of the fresh charge concentration depicted in *Figure 7b* shows that the 0.6 contours have reached the exhaust port, indicating the formation of a loop circuit connecting the scavenge ports and the exhaust port. The plume shape of the contour lines in J = 18 and 27 planes reflects the rising flow structure and the effects of the toroidal vortex. The fresh charge and the residual gas are mixing within the vortex flow.

After the scavenge ports are closed, *Figure 8a* for 240° CA shows transformation of the loop flow into a tumbling motion. The single tumbling vortex dominates the flow structure over most of the cylinder volume. The concentration (*Figure 8b*) is distributed with higher levels over the cylinder head than on the piston head. There exists direct escape of fresh charge into the exhaust port.

At 300° CA (*Figure 9a*), corresponding to the mid-compression period, the tumbling vortex is compressed by the motion of the piston and its strength has already decayed. Because of turbulent mixing, the distribution of fresh charge, depicted in *Figure 9b*, becomes rather uniform. As a result of the transport by the tumbling motion, higher levels of concentration are now distributed over the piston head rather than over the cylinder head.

By 330° CA the flow in the cylinder is further compressed. The mean flow has decayed to a large extent and the tumbling flow disintegrated (*Figure 10a*). As for the concentration, the distribution now is quite uniform with the levels in the range 0.78–0.83.

The engine speed used in the above calculation is 3000 rpm. Two other speeds, i.e. 1500 rpm and 4500 rpm, have also been tested. The temporal variation of the overall mean kinetic energy

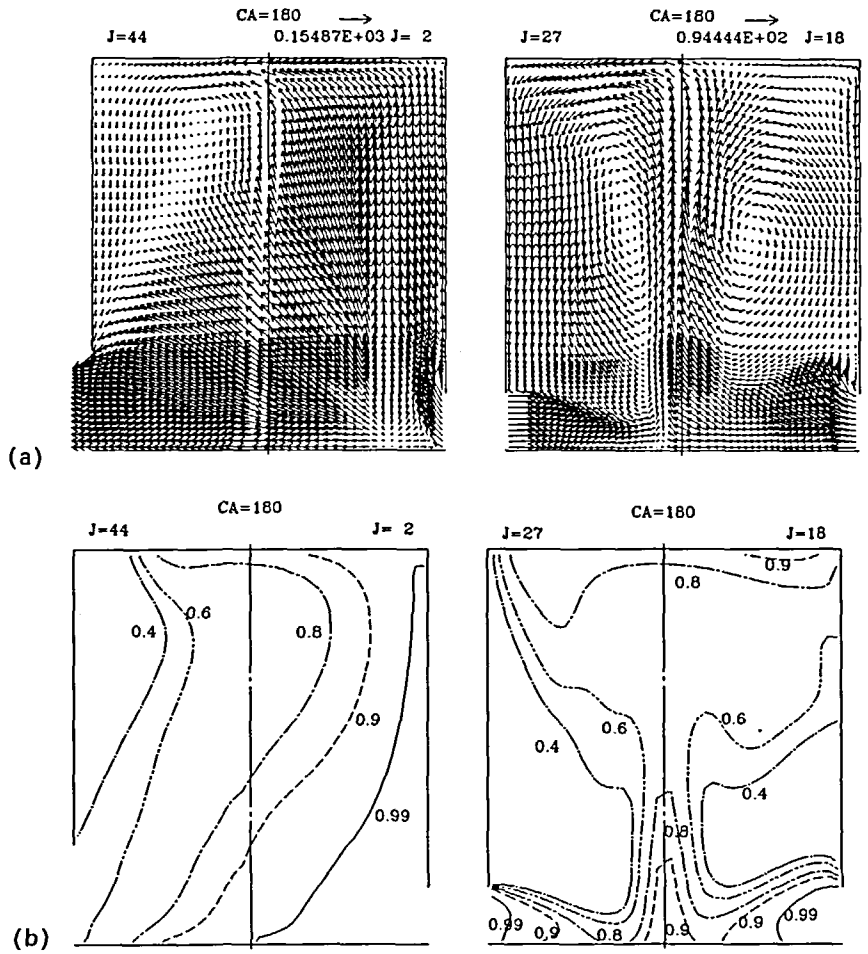

Figure 7 Flow field at 180° CA: (a) mean velocity, (b) concentration

in the entire cylinder for the three speeds is shown in *Figure 11*. The energy increases sharply during the early scavenge period because a large amount of fresh charge is introduced into the cylinder. It is then followed by a rapid decay. The decay rate slows down during the compression stroke. By the end of compression, the mean kinetic energy falls to a very low level. It is noted that during the gas exchange period the peak level is higher for the lower speed cases because more fresh charge is introduced into the cylinder for them (note that for the same time interval in terms of crank angles, the elapsed time is longer if the engine speed is lower). However the decay rate is also higher for the low engine speeds. Consequently, the energy level becomes lower after closure of the scavenge ports.

In *Figure 12* the variation of the cylinder-averaged turbulence intensity against crack angle is depicted. The values are normalized by the mean piston speed for the case of 3000 rpm ($\bar{V}_{3000} = 7.5$ m/s). Similar to the mean kinetic energy, the turbulence increases rapidly in the early scavenge stage and then declines sharply. The turbulence levels are higher for the lower speeds in the early period and fall to a lower level later. The curves tend to level off during the mid-compression stroke, followed by a sharp decrease to the end of compression. The turbulence values at TDC are about $0.3\bar{V}_{3000}$, $0.6\bar{V}_{3000}$ and $0.9\bar{V}_{3000}$ for the speeds of 1500, 3000 and 4500,

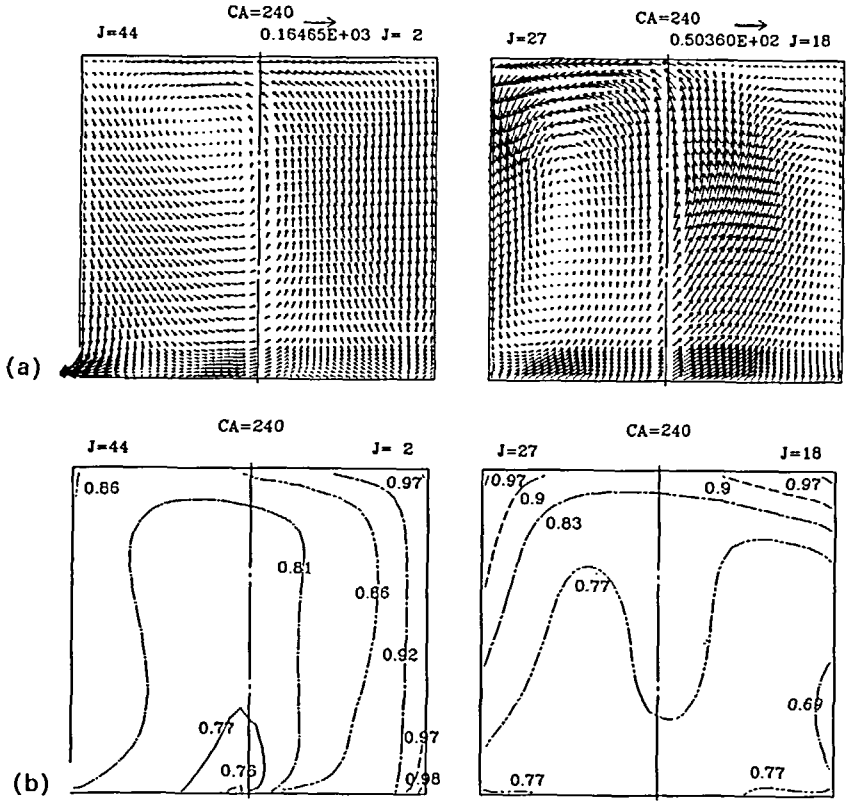

Figure 8 Flow field at 240° CA: (a) mean velocity, (b) concentration

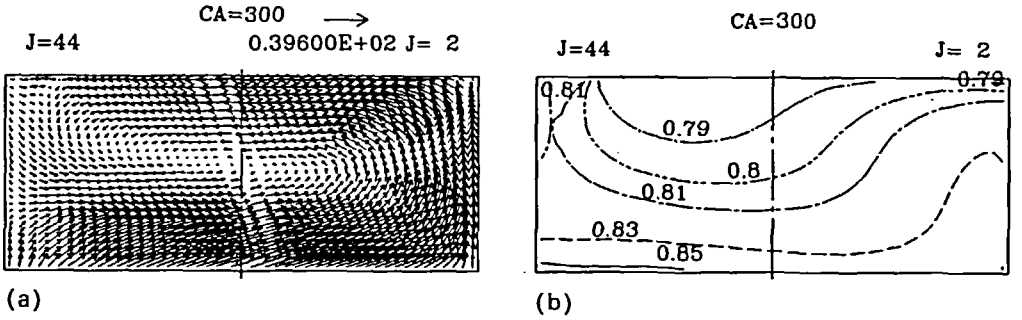

Figure 9 Flow field at 300° CA: (a) mean velocity, (b) concentration

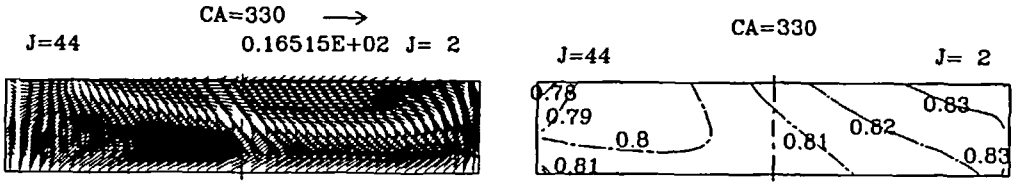

Figure 10 Flow field at 330° CA: (a) mean velocity, (b) concentration

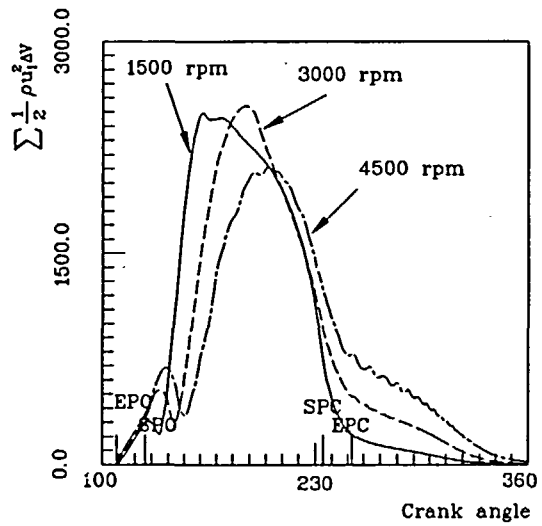

Figure 11 Comparison of mean kinetic energy for different engine speeds

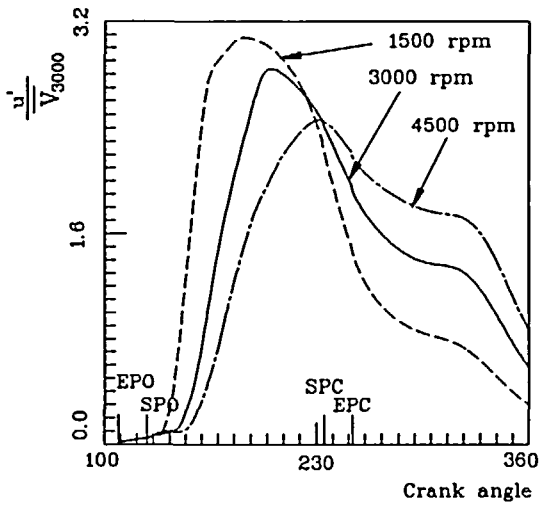

Figure 12 Comparison of mean kinetic energy for different engine speeds

respectively. Thus it can be concluded that by the end of compression, turbulence level is scaled with the engine speed and is about 0.6 times of the mean piston speed. The above results are roughly consistent with the findings in other works.[17,18,23]

The effects of discharge coefficient are examined next. In addition to the value 0.70 for the inlet C_d used above, the values 0.5 and 0.8 have also been tested. Increasing the discharge coefficient means an increase of the scavenge flow velocity. Therefore, more turbulence is generated during the scavenge period, as shown in *Figure 13*. However, the rapid decay in the later stage results in the same level of turbulence by TDC, irrespective of the discharge coefficient. The effect of the C_d on the scavenging efficiency is shown in *Figure 14*. Also presented in the same figure are the curves for the perfect displacement and perfect mixing models. As expected,

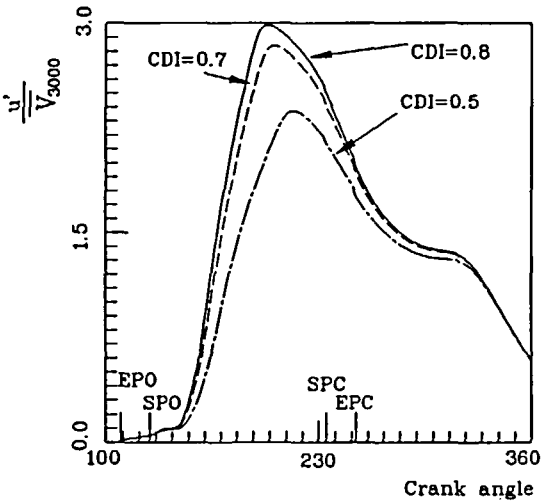

Figure 13 Comparison of mean kinetic energy for different inlet discharge coefficients

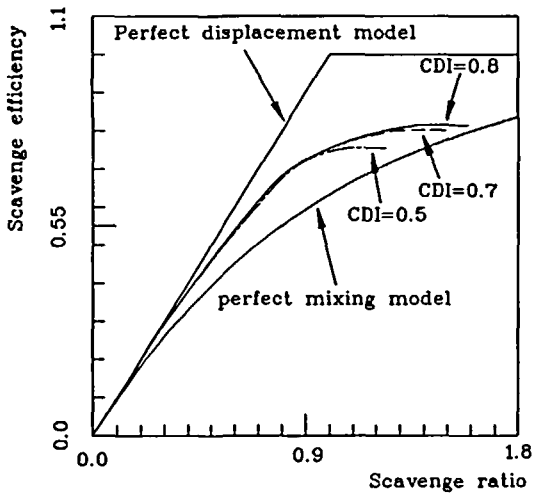

Figure 14 Comparison of mean kinetic energy for different inlet discharge coefficients

the current predictions are located within the two extreme models and the higher is the C_d value, the larger is the scavenge efficiency.

The last to study is the angle of the boost port. The value of 52.5° was used in the previous calculations. Also studied are 40°, 65° and 77.5°. It is noted that increase of the angle will cause increase of the inlet axial velocity in the calculation, but the radial velocity remains unchanged. The variations of the cylinder-averaged fresh-charge-concentration and the scavenge efficiency are displayed in *Figures 15* and *16*, respectively. In the early stage, the higher angles lead to higher scavenge efficiency and higher level of concentration because more fresh gases are directed toward the cylinder head and, thus, there is less chance for them to escape into the exhaust port. However, the order of merit is changed later due to the fact that the high-speed gases for the high angle cases loop more quickly around the cylinder, resulting in more serious

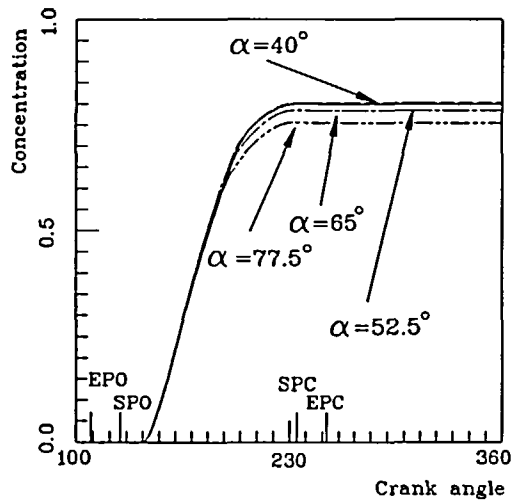

Figure 15 Comparison of concentration for different boost port angles

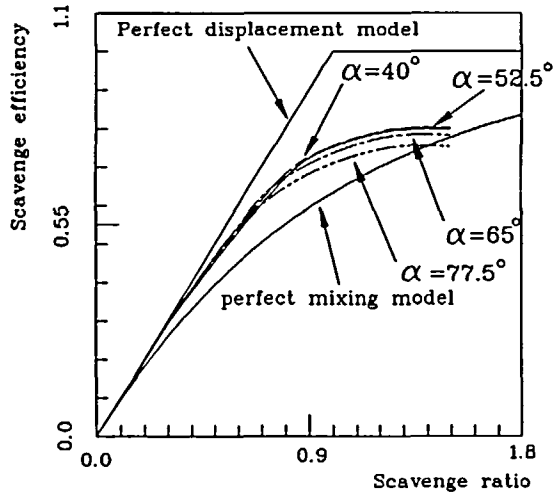

Figure 16 Comparison of scavenge efficiency for different boost port angles

short-circuiting. By the end of the scavenging process, the ones with 40° and 52.5° rank best and that with 77.5° is the worst. This indicates that optimization on the port angle is necessary for a good design. It is interesting to note that the angle 52.5° is taken from a production engine.

CONCLUSIONS

A model for the flow in a loop-scavenged two-stroke engine has been developed. The model is formulated on a moving frame such that the computational grid moves in accordance with the piston motion. The EPISO algorithm is adopted and modified as the solution method. Results

have shown the following main findings:

1. A loop circuit is formed between the scavenge ports and the exhaust port during the gas exchange period. The loop flow is transformed into a tumbling vortex after the ports are closed, which dominates the flow structure in the cylinder till the late compression period.
2. Turbulence is generated during the early scavenge period and then decays. The turbulence intensity near TDC is linearly scaled with the engine speed. By the end of compression it is about 0.6 times of the mean piston speed.
3. The inlet discharge coefficient has large effect on the efficiency of the gas exchange process. With larger discharge coefficient, the scavenge efficiency is improved.
4. The angle of the boost port also affects the scavenge efficiency. This angle needs to be optimized for design of a *good* engine.

ACKNOWLEDGEMENT

This work was supported by National Science Council under contract number NSC 81-0401-E009-503.

REFERENCES

1 Vieilledent, E. Low pressure electronic fuel injection system for two-stroke engines, *SAE Paper* 780767 (1978)
2 Douglas, R. and Blair, G. P. Fuel injection of a two-stroke cycle spark ignition engine, *SAE Paper* 820952 (1982)
3 Francisek, B. and Radislau, P. The nozzle location and the shape of its surroundings in the cylinder of small two-stroke engine, *SAE Paper* 860169 (1986)
4 Sher, E. An improved gas dynamic model simulating the scavenging process in a two-stroke cycle engine, *SAE Paper* 800037 (1980)
5 Sher, E. Prediction of the gas exchange performance in a two-stroke cycle engine, *SAE Paper* 850086 (1985)
6 Ahmadi-Befrui, B., Brandstatter, W. and Kratochwill, H. Multidimensional calculation of the flow processes in a loop-scavenged two-stroke cycle engine, *SAE Paper* 890841 (1989)
7 Sweeney, M. E. G., Swann, G. B. G., Kenny, R. G. and Blair, G. P. Computational fluid dynamics applied to two-stroke engine scavenging, *SAE Paper* 851519 (1985)
8 Spalding, D. B. A general purpose computer program for multi-dimensional one and two-phase flow, *Math. and Comp. in Simulation*, **23**, 267–276 (1981)
9 Smyth, J. G., Kenny, R. G. and Blair, G. P. Steady flow analysis of the scavenging process in a loop scavenged two-stroke cycle engine – a theoretical and experimental study, *SAE Paper* 881267 (1988)
10 Smyth, J. G., Kenny, R. G. and Blair, G. P. Motored and steady flow boundary conditions applied to the prediction of scavenging flow in a loop scavenged two-stroke cycle engine, *SAE Paper* 900800 (1990)
11 Epstein, P. H., Reitz, R. D. and Foster, D. E. Computations of a two-stroke engine cylinder and port scavenging flows, *SAE Paper* 910672 (1991)
12 Amsden, A. A., O'Rourke, P. J. and Butler, T. D. KIVA-II: A computer program for chemically reactive flows with sprays, Los Alamos National Laboratory, *Report, LA-11560-MS* (1989)
13 Gosman, A. D., Johns, R. J. R. and Watkins, A. P. Development of prediction methods for in-cylinder processes in reciprocating engines, *Comb. Mod. in Reciprocating Eng.* (Eds. J. N. Mattavi and C. A. Amann), Plenum Press, New York (1980)
14 Patankar, S. V. *Numerical Heat Transfer and Fluid Flow*, McGraw-Hill, New York (1980)
15 Gosman, A. D., Tsui, Y. Y. and Watkins, A. P. Calculation of three-dimensional air motion in model engines, *SAE Paper* 840229 (1984)
16 Gosman, A. D., Tsui, Y. Y. and Vafidis, C. Flow in a model engine with a shrouded valve – a combined experimental and computational study, *SAE Paper* 850498 (1985)
17 Gosman, A. D., Tsui, Y. Y. and Watkins, A. P. Calculation of unsteady three-dimensional flow in a model motored reciprocating engine and comparison with experiment, *Proc. Fifth Symp. on Turbulent Shear Flows*, Cornell University (1985)
18 Tsui, Y. Y. Calculation of three-dimensional flow in motored engines, *PhD Thesis*, Imperial College, University of London (1987)
19 Ahmadi-Befrui, B., Gosman, A. D., Issa, R. I. and Watkins, A. P. EPISO – an implicit non-iterative solution procedure for the calculation of flows in reciprocating engine chambers, *Comp. Meth. in Appl. Mech. and Eng.*, **79**, 249–279 (1990)

20 Issa, R. I. Solution of the implicitly discretised fluid flow equations by operator-splitting, *J. Comput. Phys.*, **62** (1), 40–65 (1986)
21 Launder, B. E. and Spalding, D. B. The numerical computation of turbulent flow, *Comp. Meth. in Appl. Mech. and Eng.*, **3**, 269–289 (1974)
22 Reynolds, W. C. Modelling of fluid motions in engines – an introductory overview, *Comb. Mod. in Reciprocating Engines* (Eds. J. N. Mattavi and C. A. Amann), Plenum Press, New York (1980)
23 Liou, T. M., Hall, M., Santavicca, D. A. and Bracco, F. V. Laser Doppler velocimetry measurements in valved and ported engines, *SAE Paper* 840375 (1984)